Particle habit in tropical ice clouds during CRYSTAL-FACE: Comparison of two remote sensing techniques with in situ observations

H. Chepfer,[1] V. Noel,[2] P. Minnis,[3] D. Baumgardner,[4] L. Nguyen,[3] G. Raga,[4] M. J. McGill,[5] and P. Yang[6]

[1]   Ice crystal shapes in tropical ice clouds are estimated with two different remote sensing methods and compared with measurements from an in situ cloud aerosol spectrometer (CAS) during the Cirrus Regional Study of Tropical Anvils and Cirrus Layers–Florida Area Cirrus Experiment (CRYSTAL-FACE) campaign conducted in Florida during July 2002. The remote sensing techniques use dual-satellite reflectances and lidar linear depolarization rates. The ice crystal shape is derived from CAS measurements of forward and backscattered light from individual particles in the size range from 1 to 45 μm. The remote sensing and in situ retrievals are based on ice crystal optical models, which incorporate the scattering phase functions integrated over the collection angles used by the CAS, the view angles from dual-satellites retrievals, and the complete scattering matrix for lidar. Owing to the space and time collocation constraint between in situ and remote sensing techniques, data from only 1 day are used to evaluate the dual-satellite technique (11 July) and from 3 days for the lidar (23, 26, and 29 July). Data from 23 and 29 July are also used to compare the two remote sensing techniques. In total, 40 shape retrievals were obtained for 20 different cloud areas, allowing paired comparisons of the methods. The results show consistent particle shapes for half of the cloud areas studied. The discrepancies for the other cases can be explained by insufficient spatial-temporal collocations of the data or limitations of the CAS that constrain its range to particles <45 μm, whereas the remote sensing techniques are influenced by particles outside the size range of the CAS.

1.   Introduction

[2]   Ice clouds play a major role in the atmospheric energy balance [*Liou*, 1986; *Stephens et al.*, 1990] through their albedo and greenhouse effects. The determination of ice cloud microphysical and macrophysical properties from in situ and remote sensing observations remains a challenging task. Ice cloud microphysical properties such as particle size, shape and orientation vary in space and time yet must be accurately characterized since they influence the cloud interactions with radiation. In the shortwave radiative domain, the relative fraction of light scattered in the upward and downward hemispheres is sensitive to the particle shape. For example, simple plane-parallel radiative transfer computations demonstrate that cloud albedo can be modified as much as 20% at a constant ice water content for the same cloud composed of various particle habits. Improving our knowledge of particle habits in various locations and times is the goal of numerous studies using in situ observations collected during several intensive field experiments [e.g., *Randall et al.*, 1996; *Raschke et al.*, 1998; *McFarquhar and Heymsfield*, 1996; *Toon and Miake-Lye*, 1998] and recently the Cirrus Regional Study of Tropical Anvils and Cirrus Layers–Florida Area Cirrus Experiment (CRYSTAL-FACE). The results of these in situ analyses illustrate the large variability of particle shape [e.g., *Heymsfield*, 1975; *Heymsfield and Platt*, 1984; *Heymsfield*, 1993; *Francis et al.*, 1994], and highlight potential links between the crystal habit and the latitude, and atmospheric temperature and humidity. Those studies also show that the particle microphysical properties, if averaged over the entire globe, are probably not particularly

---

[1]Laboratoire de Météorologie Dynamique, Institut Pierre-Simon Laplace, Palaiseau, France.
[2]Analytical Services and Materials, Inc., Hampton, Virginia, USA.
[3]NASA Langley Research Center, Hampton, Virginia, USA.
[4]Centro de Ciencias de la Atmósfera, Universidad Nacional Autónoma de México, Mexico City, Mexico.
[5]NASA Goddard Space Flight Center, Greenbelt, Maryland, USA.
[6]Department of Atmospheric Sciences, Texas A&M University, College Station, Texas, USA.
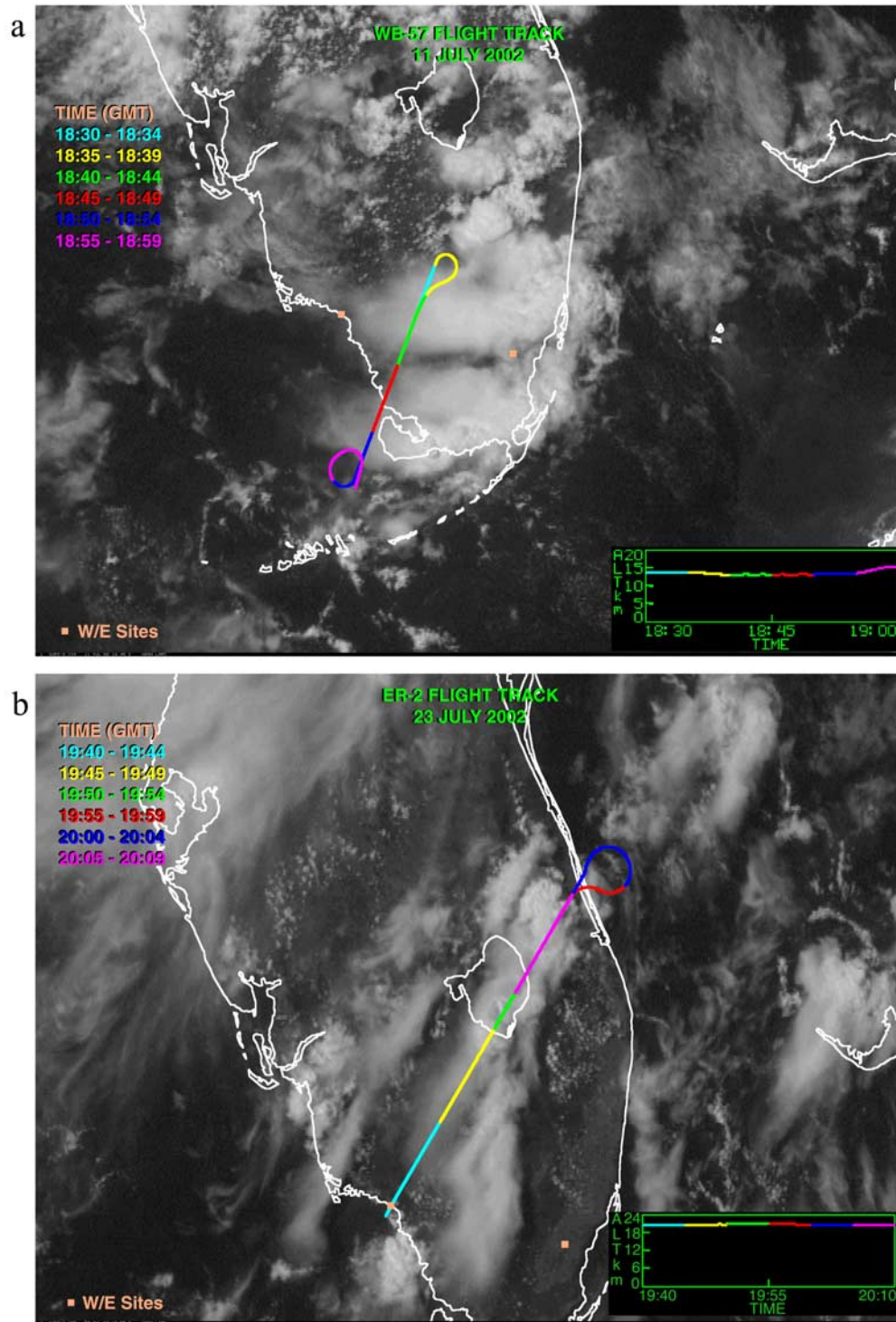
Figure 1. Cloud areas selected for dual-satellite retrieval method as seen by GOES 8. The line represents the WB57 flight track: (a) 11 July and (b) 23 July.

relevant to understanding the physical processes underlying crystal formation at specific latitudes under different dynamical environments.

[3] Some remote sensing methods have been developed to detect signatures of variations in ice cloud microphysical properties, so that global satellite coverage can be used to develop a better description of those properties at various latitudes and time periods. These methods start with estimates of the ice crystal sizes [*Inoue*, 1985; *Minnis et al.*, 1993, 1998; *King et al.*, 2003; *Platnick et al.*, 2003] using both geostationary and low-orbiting satellites. More recently, active remote sensing techniques have been developed to utilize ground based active observations [*Intrieri et al.*, 1993; *Mace et al.*, 2002]. More recent efforts have been

Table 1a. Satellite and In Situ Data for Goes 8 (G8) and NOAA 16 (N16)

Date	Area	UTC	Complementary Information	In Situ UTC
		Satellites		
11 July	Z0 25.3/81.15	1833 (G8), 1826 (N16)	$\theta_{s\text{-}G8} = 11.8°$, $\theta_{v\text{-}G8} = 30.4°$, $\phi_{v\text{-}G8} = 91.1°$; $\theta_{s\text{-}N16} = 10.85°$, $\theta_{v\text{-}N16} = 58.3°$, $\phi_{v\text{-}N16} = 180°$	1836–1840
11 July	Z1 25.85/80.95	1833 (G8), 1826 (N16)	$\theta_{s\text{-}G8} = 12.1°$, $\theta_{v\text{-}G8} = 30.6°$, $\phi_{v\text{-}G8} = 89.6°$; $\theta_{s\text{-}N16} = 11.2°$, $\theta_{v\text{-}N16} = 57.2°$, $\phi_{v\text{-}N16} = 179.4°$	1850–1855
11 July	Z2 and Z3 25.9/80.85	1833 (G8), 1826 (N16)	$\theta_{s\text{-}G8} = 12.2°$, $\theta_{v\text{-}G8} = 31°$, $\phi_{v\text{-}G8} = 87.7°$; $\theta_{s\text{-}N16} = 11.3°$, $\theta_{v\text{-}N16} = 56.9°$, $\phi_{v\text{-}N16} = 177.4°$	1862–1870

directed toward deriving ice crystal shape from remote sensors, or at least estimating the asymmetry factor that is the link between the crystal habit and its radiative impact on the albedo. The methods developed to retrieve information about the crystal shape [*Baran et al.*, 1999; *Chepfer et al.*, 1998; *Noel et al.*, 2001; *Masuda et al.*, 2002; *Chepfer et al.*, 2002] usually utilize visible wavelengths because the signature of variations in crystal habit is dominant at those wavelengths in comparison with the infrared or millimeter domain. Some techniques use bidirectional reflectance observations to detect different signatures linked to the scattering phase function depending on the crystal shape, or observations of the state of polarization of light scattered by the particle, another parameter strongly dependent on the crystal shape.

[4] The goal of this paper is to compare the shapes of crystals in tropical clouds derived from satellites and lidar to in situ measurements in order to assess the capability of remote sensors to resolve crystal shapes. The first technique [*Chepfer et al.*, 2002] uses dual satellite observations and takes advantage of bidirectional reflectance signatures. The second method [*Noel et al.*, 2001, 2004] is based on the depolarization ratio observed in lidar backscattering. The in situ retrieval takes advantage of bidirectional light scattering measurements of single particles made with the cloud aerosol spectrometer (CAS) [see *Baumgardner et al.*, 2005]. The two remote sensing techniques are applied to small data sets collocated in space and time with in situ observations taken during the CRYSTAL-FACE campaign [*Jensen et al.*, 2004] conducted between 1 and 30 July 2002 over Florida and the Gulf of Mexico. In the future, the dual satellite technique can be applied to collocated observations by geostationary and low-orbiting satellites, whereas the lidar technique can be applied to space-borne lidar with polarization capabilities [*Winker et al.*, 2003] leading to global maps of the particle shape and visible wavelength asymmetry factors. This paper provides the first in a series of validation efforts for these two potentially valuable remote sensing methods.

2. Observations

[5] The current data set was collected in tropical ice clouds during the CRYSTAL-FACE campaign in July 2002. The cloud cases examined here correspond to times when the satellite and/or ER-2 remote sensing observations were collocated in the same cloud area to within 24 km of the WB57F aircraft. The matching requires that the WB57F flies through cirrus clouds during the NOAA 16 or Aqua overpasses and that the scattering angle between the target and the advanced very high-resolution radiometer

(AVHRR) or Moderate Resolution Imaging Spectroradiometer (MODIS) is sufficiently different from that between the target and the Geostationary Operational Environmental Satellite (GOES) imager.

2.1. Dual-Satellite Data

[6] In the dual-satellite technique, a given cloud area is observed by two satellites from different directions. For both satellites, the radiances are measured at 650 nm, collocated in space and time (less than 15 min difference) and intercalibrated as given by *Minnis et al.* [2002]. For CRYSTAL-FACE (CF), the two satellite sensors are the GOES 8 (G8) imager and the NOAA 16 (N16) AVHRR or the G8 imager and Aqua MODIS. During the N16 and Aqua overpasses, the solar zenith angle generally varied between 10° and 30°. The cloud areas were observed at scattering angles around 150° and 110°. The WB57F aircraft, which carries the CAS, passed through cirrus clouds during the 11 July N16 overpasses and during 23 and 29 July under the ER-2 aircraft, which carried the lidar. A thin cloud was sampled above Florida (Figure 1a) during 11 July around 1830 UTC. The mean G8 infrared (IR) brightness temperatures for three different WB57F flight segments, designated Z0, Z1, and Z2, are 240 K, 223 K, and 213 K, respectively. These segments are considered separately for comparison with the in situ data. On 23 July the WB57F sampled a thick ice cloud above Florida just before 2000 UTC. Two different cloud segments with IR temperatures lower than 222 K were collocated with the ER-2 flight track (Figure 1b) and used for comparisons with lidar retrievals. At 1920 UTC, 29 July (not shown), the WB57F flew through a thick cloud along the ER-2 flight track above the Gulf of Mexico off the Florida peninsula. The satellite viewing directions for each case study are given in Tables

Table 1b. Lidar and In Situ Data for G8 and N16

Date	Area	UTC	Complementary Information	In Situ UTC
		Lidar		
23 July	24.42/81.02	1972–1974	z = 13.18 km	1972–1974
	80.95/26.62	1978–1982	13.18–13.50	1978–1982
	81.27/26.02	2023–2032	14.40	2023–2032
	81.15/26.22	2116–2122	13.20	2116–2122
	81.44/25.75	2167–2175	13.80	2167–2175
	81.70/27.00	2216–2217	14.60	2216–2217
	81.56/25.57	2257–2262	13.50	2257–2262
	80.85/26.70	2305–2320	13.50–12.80	2305–2320
26 July	85.80/21.13	1740–1743	z = 15.70–15.90 km	1740–1743
	83.10/15.50	1828–1851	15.20–15.70	1828–1851
	83.45/16.40	1901–1914	13.00–14.75	1901–1914
	83.75/17.00	1916–1921	15.20–15.90	1916–1921
29 July	82.63/26.65	1988–1993	z = 12.5 km	1988–1993

Table 1c. Satellite and Lidar Data for G8 and N16

Date	Area	UTC	Complementary Information	Lidar UTC
		Satellite		
23 July	Z1 80.80/26.75	1961 (G8), 1943 (N16)	$\theta_{s\text{-}G8} = 29.9°$, $\theta_{v\text{-}G8} = 32°$, $\phi_{v\text{-}G8} = 96.2°$; $\theta_{s\text{-}N16} = 27.6°$, $\theta_{v\text{-}N16} = 45°$, $\phi_{v\text{-}N16} = 1.3°$	19.81–19.84
23 July	Z2 80.50/27.15	1961 (G8), 1943 (N16)	$\theta_{s\text{-}G8} = 30.2°$, $\theta_{v\text{-}G8} = 32.4°$, $\phi_{v\text{-}G8} = 94.9°$; $\theta_{s\text{-}N16} = 27.9°$, $\theta_{v\text{-}N16} = 46.5°$, $\phi_{v\text{-}N16} = 2.0°$	19.89–19.92
29 July	Z1 80.80/26.75	1932 (G8), 1918 (Aqua)	$\theta_{s\text{-}G8} = 24.9°$, $\theta_{v\text{-}G8} = 32.15°$, $\phi_{v\text{-}G8} = 92.3°$; $\theta_{s\text{-}N16} = 23°$, $\theta_{v\text{-}N16} = 42.5°$, $\phi_{v\text{-}N16} = 8.8°$	19.18–19.22

1a–1c. The satellite data were averaged along the WB57F and the ER-2 flight tracks in three different super pixels covering areas with boxes of 3 × 3 km, 18 × 18 km and 36 × 36 km.

2.2. Lidar Airborne Data

[7] The cloud physics lidar (CPL) [*McGill et al.*, 2004] is an airborne Nd-YV04 lidar with polarization capabilities that was onboard the ER-2 aircraft during the CF mission. This study uses its observations of linear depolarization ratio (Δp) at 1064 nm, defined as the ratio of backscattered intensities in the plane of polarization perpendicular and parallel to the one of the linearly polarized source. The ability of the depolarization ratio to distinguish between liquid water clouds (composed of spherical water droplets) and solid ice clouds (composed of nonspherical ice particles) recognized very early [*Pal and Carswell*, 1976; *Platt*, 1977] and has been used in cloud phase retrievals ever since. This capability has been attributed to a high sensitivity to the shape of hydrometeors in the probed cloud [*Sassen*, 1991], which was reproduced and extensively studied through light scattering models [*Takano and Liou*, 1989; *Macke*, 1993; *Yang and Liou*, 1996]. Moreover, the depolarization ratio was shown to be independent of particle size, except for particle sizes equivalent to or smaller than the lidar wavelength [*Mishchenko and Sassen*, 1998]. This capability has been used in multiple studies of ice cloud microphysical properties [*Eberhard*, 1992; *Stefanutti et al.*, 1995] and is the basis for the lidar shape classification method used in the present study (section 3.2).

[8] Figure 2 shows the cloud sequences as observed by the CPL in polarization, and the collocated WB57 flight track within the cloud. The vertical and temporal resolutions are 30 m and 1s, respectively. Data from 23, 26, and 29 July are compared with the CAS retrievals. Eight, three, and one flight segments were selected for 23, 26, and 29 July, respectively. The time difference between the ER-2 and the WB57F is less than 10 min, and the space collocation is better than 2 km. The lidar retrievals are extracted for the portion of the cloud at the altitude of the WB57. Three complementary cloud segments taken from 23 and 29 July data were selected for comparison with the dual satellite retrievals. The different segments are summarized in Tables 1a–1c.

2.3. In Situ Data

[9] Various in situ probes participated in the CF mission. Using several probes from two aircraft, *Garrett et al.* [2003] demonstrated that small ice crystals (sizes lower than 50 μm) were dominant in CF clouds. To help overcome the difficulties in measuring small ice crystal in cirrus clouds, *Baumgarnder et al.* [2005] proposed a method to derive the shape of those small crystals using CAS observations. The CAS [*Baumgardner et al.*, 2001] observes particles with diameters ranging between 1 and 45 μm. It measures forward and backward light intensity scattered by individual particles that pass through a laser (λ = 680 nm). The forward cone of light is between 4° and 12°, and the backscattering cone between 168° and 176°. The CAS was mounted on the left wing of the NASA WB57F aircraft during CF. Eighteen CAS segments, collocated in space and time with remote sensing observations, are used in the current study (Tables 1a–1c).

3. Retrieval Methods

[10] This section summarizes the different methods used to derive particle shape. More information on each method is provided by *Chepfer et al.* [2002] for the dual-satellite method, *Noel et al.* [2002] for the lidar approach, and *Baumgardner et al.* [2005] for the CAS technique.

3.1. Ice crystal Optical Properties

[11] The remote sensing and in situ methods interpret measurements of light scattered in the visible domain using theoretical ice crystal optical properties. In this wavelength domain, pure ice scatters light conservatively. When the particle size is larger than 10 μm, the theoretical properties (including the scattering phase function and the complete scattering matrix) are computed in the framework of geometric optics approximation enhanced with Fraunhofer diffraction. Geometric optics is independent of the particle size, unlike Fraunhofer diffraction. As a consequence, when the scattering angle is larger than 3°, where the main diffraction peak is negligible, the scattering phase function (and scattering matrix) is less dependent on particle size. However, the secondary diffraction peaks still have some influence but at a smaller level. The in situ and two remote sensing methods use the phase function (or scattering matrix) at various scattering angles ranging between 4° and 180°; hence the information obtained with those methods is mainly a signature of the particle shape when the size of the particles under study exceeds 10 μm. During the CF campaign, a large quantity of particles smaller than 10 μm were observed, so optical properties computed with the finite difference time domain method, which is adapted for small particles, are also considered in the current study. The phase function obtained with this computation method is strongly sensitive to the particle size in small scattering angles but is still mainly sensitive to crystal shape at large angles. Hence the in situ retrieval, which uses observations in both scattering angle ranges (4°–12° and 168°–176°), will be sensitive to both particle size and shape, whereas the retrievals based on observations at large scattering angles
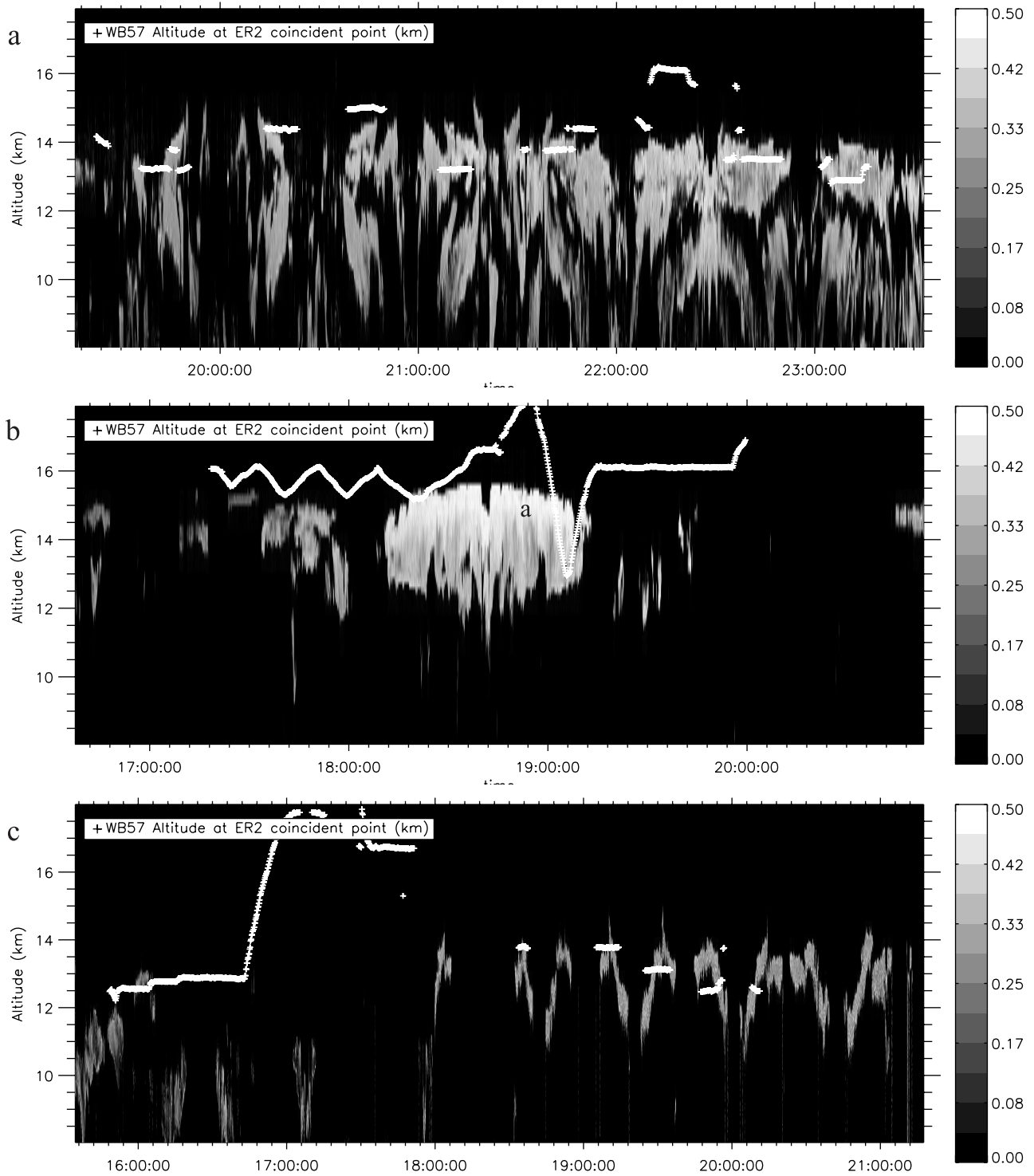
Figure 2. Cloud areas selected for lidar retrieval, as seen by the cloud physics lidar onboard the ER-2. The line represents the WB57 flight track: (a) 23 July, (b) 26 July, and (c) 29 July.

(>110° for satellites, around 180° for lidar) are primarily sensitive to particle shape only.

[12] Twenty state-of-the-art randomly oriented ice crystal models in the visible domain are summarized in Table 2. They contain simple monomodal ice crystals and more complex ones composed of mixed of particles. The detailed algorithms for computing the single-scattering properties of

these particles can be found in the literature [e.g., *Wendling et al.*, 1979; *Takano and Liou*, 1989; *Macke et al.*, 1996; *Yang and Liou*, 1996, 1998; *Noel et al.*, 2001]. For the MODIS models in Table 2, the population of ice crystals consists of various ice crystal habitats with certain percentages [*Baum et al.*, 2000; *King et al.*, 2004]. Note that the Cloud and the Earth's Radiant Energy System (CERES)

Table 2. Ice Crystal Models[a]

Name	Crystal Shapes	Q_{eq}	g	D	M(180)	R_{CAS}
COL-a	hexagonal columns	2.5	0.80	40	Y	4
COL-b	hexagonal columns	2	0.81	7.5	N	117
COMPa	hexagonal compacts	1	0.70	40	N	5
COMPb	hexagonal compacts	1	0.74	100	Y	2.5
COMPc	hexagonal compacts	1	0.76	5	N	84
PL1a	hexagonal plates	0.05	0.85	40	N	25
PL1b	hexagonal plates	0.05	0.90	100	Y	11
PL2	hexagonal plates	0.7	0.74	100	Y	3
BR	bullet rosettes	1	0.83	87	N	18
CERES-Big	hexagonal compacts plus columns	>1	0.85	135	N	6
CERES-Nov	hexagonal compacts plus columns	>1	0.82	75	N	7
CERES-Cont	hexagonal compacts plus columns	>1	0.77	18	N	29
MODIS-1	bullet rosettes plus plates plus hollow columns plus aggregates	-	0.75	9	N	39
MODIS-2	bullet rosettes plus plates plus hollow columns plus aggregates	-	0.80	33	N	36
MODIS-3	bullet rosettes plus plates plus hollow columns plus aggregates	-	0.84	79	N	37
MODIS-rough	bullet rosettes plus plates plus hollow columns plus aggregates			30	N	108
ISCCP	polycrystals	1	0.70	60	N	66
Droxtal_a	droxtal	-	0.75	4	N	131
Droxtal-b	droxtal	-	0.76	6	N	90
Spheres 6	spheres	-	0.94	12	Y	60

[a]Q_{eq} is the mean equivalent shape ratio (length divided by diameter), g is the asymmetry factor, and D is the particle diameter in microns. The complete scattering matrix in backscattering M(180) is carefully computed (Y) or not (N).

[*Minnis et al.*, 1998] and MODIS models correspond to different particle size distributions. Within these mixed distributions, the smallest ones (CERES-cont (particle model used for contrails) and MODIS 1) include particles smaller than 10 μm. According to in situ observations [e.g., *Auer and Veal*, 1970], the dominant aspect ratio of small pristine ice crystals is approximately one (i.e., the compact ice crystals). Droxtals have been observed within ice fog and ice clouds [*Thuman and Robinson*, 1954; *Zhang et al.*, 2004]. This type of ice crystals has the basic hexagonal structure. However, a droxtal ice crystal has 20 faces instead of a geometry of a well-developed hexagonal column to plate. In this study, we consider four monocrystal models corresponding to particles smaller than 10 μm: Compact-C and Columns-B [*Takano and Liou*, 1989], droxtal-4 μm and droxtal-6 μm [*Yang et al.*, 2003; *Zhang et al.*, 2004]. Two spherical crystal models (diameter 12 μm and 6 μm) computed with Mie theory are also considered as a reference. Figure 3 illustrates the variation in the scattering phase function for four different crystals types.

3.2. Dual-Satellite Retrieval Method

[13] This method simulates radiances at the top of the atmosphere in the viewing directions of the two satellites for clouds composed of the different particle types summarized in Table 2 and for various optical depths ranging between 1 and 100, using an adding-doubling radiative transfer code [*De Haan et al.*, 1986]. The theoretical ratio, Rsat_t, between the radiances in the two viewing directions is computed. Because of differences in the phase function between the two directions around scattering angles of 150° and 110°, the value of Rsat_t ranges between 0.8 and 1.2 depending on the viewing directions. This simulated ratio can be directly compared to the one measured with the two satellites in order to select the phase functions consistent with the dual-satellite observations. All the mod-

els listed in Table 2 can be tested because this method requires only the scattering phase function for the radiative transfer calculations.

[14] This method has been previously applied to 28 ice cloud cases studied over North America and the Atlantic Ocean [*Chepfer et al.*, 2002] to observe variations in the ice particle shapes, but has never been validated against in situ observations. Similar methods have been applied previously to the POLDER data set [*Baran et al.*, 1999; *Chepfer et al.*,
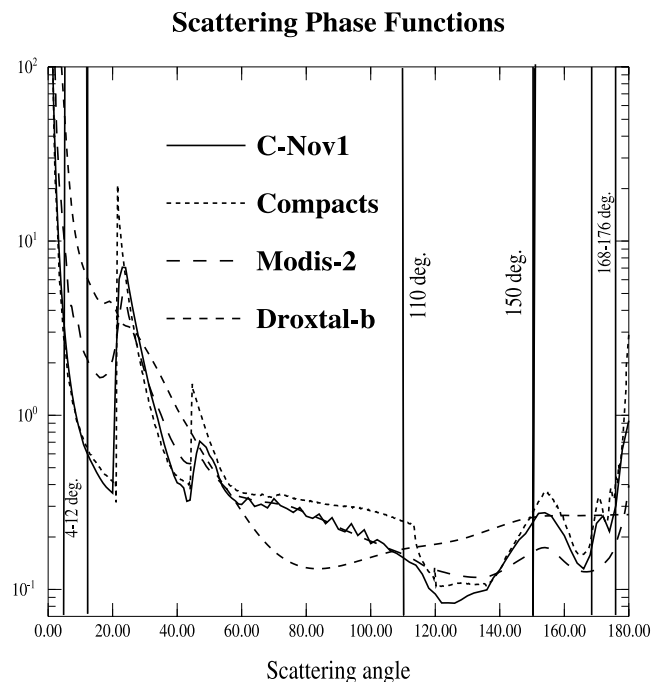
Figure 3. Examples of scattering phase functions.

1998, 2001; *Masuda et al.*, 2002] but never been validated in the tropics.

3.3. Lidar Depolarization Classification Method

[15] The diversity of particle shapes in cirrus clouds is almost infinite. As multiple shapes can produce the same depolarization ratio Δp, it is impossible to retrieve precise information about particle shape based on Δp alone. However, the shape information conveyed by Δp can be used to classify particles into broad shape categories.

[16] To evaluate the sensitivity of the depolarization ratio (Δp) to the microphysical properties of a probed cloud, a ray-tracing simulation was used to follow the lidar laser beam as it travels through various ice crystal models, recording any modification of its polarization state during the process. The depolarization ratio was then extensively studied [*Noel et al.*, 2001, 2002] as a function of the particle index of refraction ($m_r = 1.33 - 1.31$ and $m_i = 1e-9 - 1e-6$), orientation in space, shape and size. The sensitivity studies revealed that changes in the index of refraction or the particle size do not have noticeable effects on Δp. However, particle orientation is important, as horizontally oriented particles produce a unique signature of high backscattering and low depolarization ratio ($\Delta p < 0.1$), a behavior confirmed by field experiments [*Platt et al.*, 1978]. When such a signature is observed, the sensitivity to particle shape is lost and the lidar classification method cannot be used. In the present study, great care was taken to ensure that such observations were not present in the lidar data set, so random orientation could be safely assumed. Finally, in the presence of randomly oriented particles, Δp appears to be highly sensitive to the particle aspect ratio Q. It is important to recognize that because the evolution of Δp with Q is not always monotonous, it is not possible to link an observed Δp to a specific particle aspect ratio. However, given a observed Δp, a range of probable values for Q can be estimated (Table 2), and crystals can be classified into four different shape ratios. Thin, plate-like particles ($Q < 0.05$) produce low Δp in the same range as spherical particles, so both shapes are equivalent in the classification scheme (Class 1). Columnar particles ($Q > 1.05$) typically produce large values ($\Delta p > 0.5$, Class 4), while intermediate aspect ratios (irregular and intermediate shapes) are separated into thick plates ($0.05 < Q < 0.7$, Class 2) and unity aspect ratios ($0.7 < Q < 1.05$, Class 3). Each class is associated with a different asymmetry factor in the visible domain. This method gives access to information about the vertical variability of the particle shape within the cloud, since it can be applied to each altitude level detected by the lidar between the cloud top and an optical depth of 3.

[17] This method has been previously applied to 15 midlatitude ice cloud cases observed with a ground-based lidar [*Noel et al.*, 2002] at the Site Instrumente de Recherche par Teledetection Atmospherique (SIRTA) site in Palaiseau, France [*Haeffelin et al.*, 2005], with results showing good agreement with in situ observations from previous field experiments [*Korolev and Hallett*, 2000]. More recently, this technique has been applied to tropical cirrus clouds observed during CF [*Noel et al.*, 2004]. Results of the classification show a good agreement with collocated in situ observations from the cloud particle imager airborne probe.

In the presence of high optical depths, the influence of multiple scattering [*Hu et al.*, 2001] must be evaluated through additional simulations; however, in the present study, the small lidar footprint on the observed clouds (~1 m) means multiple scattering effects can be safely neglected [*Eloranta*, 1998].

3.4. CAS Retrieval Method

[18] The method consists of computing the theoretical ratio between the intensity scattered in the forward ($4°-12°$) and backward ($168°-176°$) directions for the different particle models summarized in Table 2. This theoretical ratio, ranging between 2.5 and 183, is directly compared to the measured one in order to select the most closely associated ice crystal model. All the models shown in Table 2 can be tested, as this method requires only the scattering phase function. This technique gives direct information useful for constraining the crystal model, but it is valid only for particles with sizes ranging between 1 and 45 μm. The CAS method has been applied to the complete CF data set composed of 10 flights of the WB57F aircraft [*Baumgardner et al.*, 2005], showing that in the size range of the CAS, droxtals, mixtures of bullet rosettes, hollow columns and plates (MODIS-rough model) are dominant, but 10% of the particles correspond to small columns. This retrieval method has not yet been compared to other in situ or remote sensing retrievals of particle shapes.

4. Results
4.1. Dual-Satellite Results
4.1.1. 11 July Case

[19] The dual-satellite method was applied to a cloud area observed above Florida during 11 July. This cloud is thin and heterogeneous. The satellite viewing angles vary by only ±0.5° and the time difference between G8 and N16 is 5 min. The cloud is separated in four areas (Z0–Z3), the first one with temperatures ranging between 225 and 222 K, and the others with mean temperatures of 213 K. The comparisons between the simulated and observed radiances are plotted in Figures 4a and 4b for Z0 and Z3: the theoretical ratio between the G8 and N16 radiances is shown as a function of the radiance observed in the G8 direction. Each data point corresponds to 36×36 km^2. The column model is the most appropriate to explain the measurements in area Z1; similar behavior was observed for Z1 and Z2 (not shown). Figure 4b shows that the last area (Z3) is more consistent with the spherical model.

4.1.2. 23 July Case

[20] The time difference between G8 and N16 is 15 min and two cloud areas are examined: Z1 with $T = 215$ K and Z2 with $T = 220$ K. Figure 4c illustrates the comparison of observations and simulations for the first area, with satellite data averaged over 3, 18 and 36 km along the ER-2 flight track. Figure 4c clearly illustrates the need to average the data over 36 km for a reasonable comparison because of the time difference between the two satellites. This behavior is confirmed by the other case studied (not shown) and all the satellite retrievals use the 36×36 km satellite observations. For Z1, the column model is best suited to explain the observations, whereas for Z2 the spherical model is more appropriate.
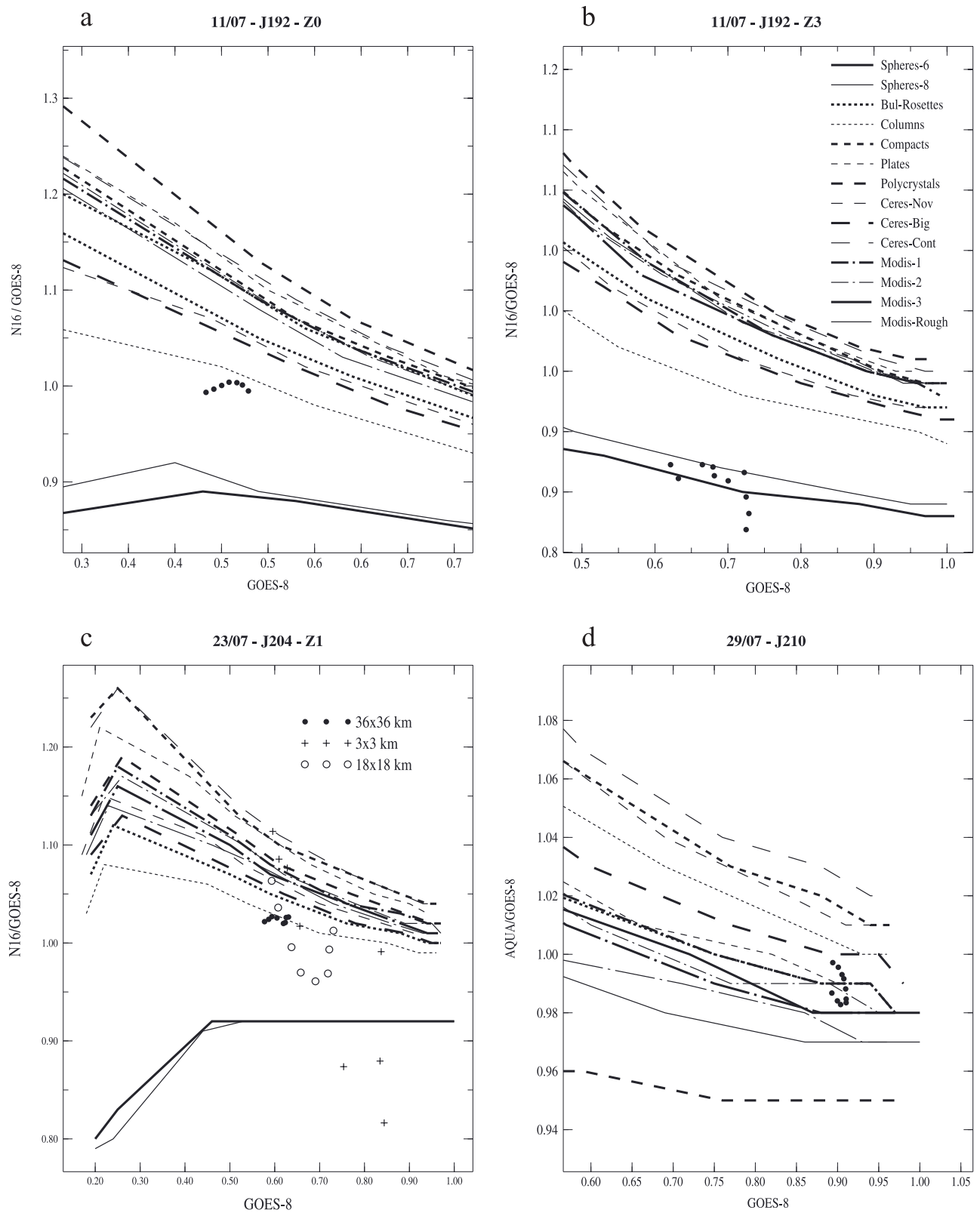
Figure 4. Dual-satellite method. Theoretical computation in line and measurements in dots: (a) 11th area 1 GOES 8/NOAA 16, (b) 11th area 3 GOES 8/NOAA 16, (c) 23rd area 1 GOES 8/NOAA 16, and (d) 29th GOES 8/Aqua.
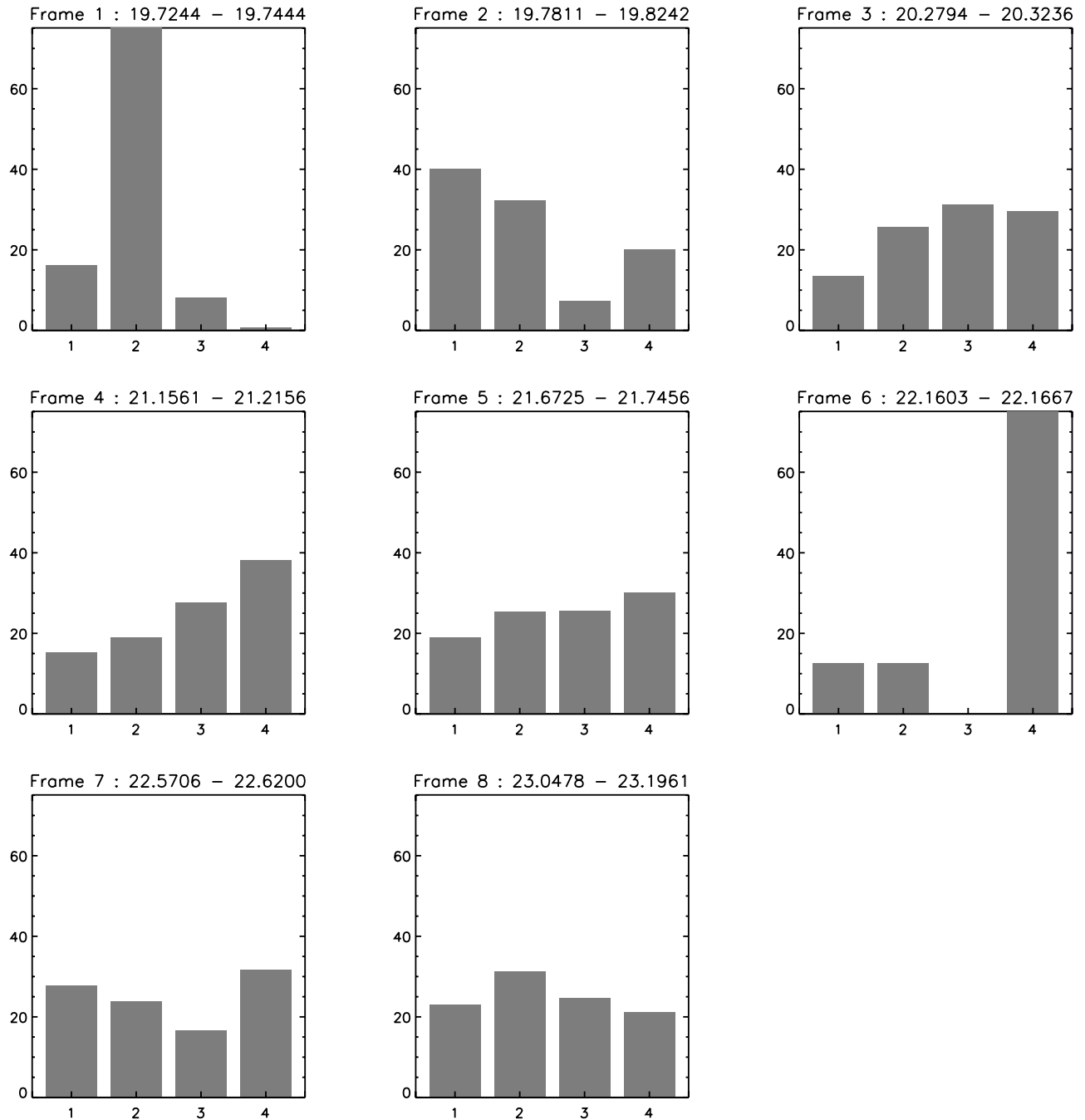
Figure 5. Lidar method. Histogram of particle shape ratio retrieved along the WB57 aircraft: 23th segments 1−8.

4.1.3. 29 July Case

[21] The time difference between G8 and Aqua is 10 min and T = 219 K. Figure 4d shows that theoretical ratios corresponding to a mixture of plates, bullet rosettes and hollow columns are most consistent with the satellite observations.

4.2. Lidar Results

[22] The lidar shape ratio retrievals were performed along the WB57F flight track with a collocation of less than 10 min and 2 km. Figure 5 shows an example of the histograms of shape ratio obtained for the different cloud segments selected for 23 July (Tables 1b and 1c). Segments

1−3 are dominated by ice crystals associated with shape ratios less than one, while class 4, associated with large shape ratios (>1), is observed most often for segments 4−7. Class 1, identified for 40% of segment 2, can be associated with spherical water particles, frozen droplets, or very thin ice plates with $Q < 0.05$. Segments 5, 7, and 8 show a somewhat uniform mix of particles in all four classes. Data from the 26 July (not shown) yield more than 80% spherical or thin plates particles for segment 1, and a predominance of ice crystals having $Q \geq 1.0$ for segments 2−4. The single segment taken during 29 July is dominated by a plate-like shape ratio (class 2) that coexists with other particles.
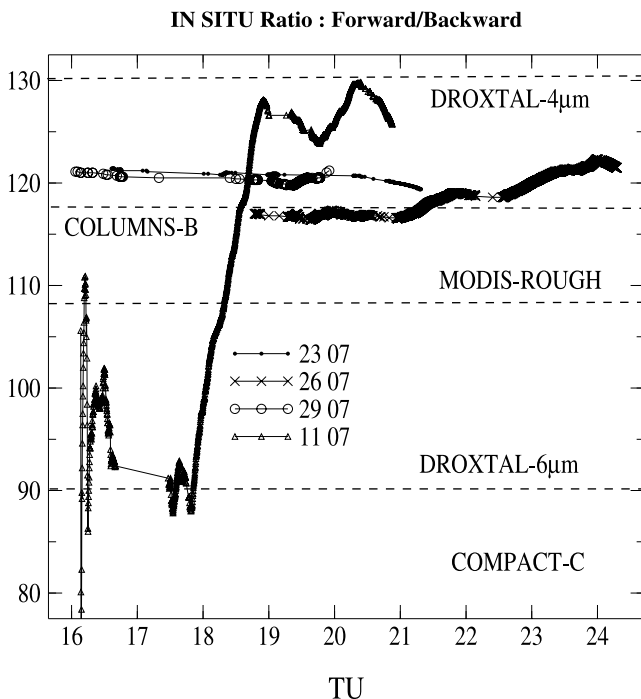
Figure 6. In situ method. Forward to backscattering ratio as measured by the cloud aerosol spectrometer as a function of time and theoretical computed ratio (horizontal line).

[23] For the 23 and 29 July segments, selected for comparisons with satellite retrievals, the lidar retrievals were processed for the complete vertical structure of clouds seen by the lidar in the same latitude/longitude area as considered for the satellite. The data for 23 July are separated into two cloud areas. For the first one, the lidar retrieval is dominated by $Q < 1$, while lidar data for the second one indicate a mixture of spherical and small shape ratios. The 29 July results are also dominated by particles with shape ratios less than unity mixed with a significant quantity of thin plates or spheres.

4.3. CAS Results

[24] The comparisons between measured and simulated forward-to-backscattering ratios (R_{CAS}) are plotted in Figure 6 for the 4 days under study. The horizontal line corresponds to the closest models. All measured values of R_{CAS} range between 80 and 130, hence the ice crystal models associated with smaller values of R_{CAS} such as MODIS-1, MODIS-2, MODIS-3, CERES-cont, CERES-Nov, CERES-Big, International Satellite Cloud Climatology Project, Spheres-6, large monocrystals (columns-a, compacts-a,-b, plates, bullet rosettes) are not plotted in Figure 6 because they are poor candidates to explain the observations.

[25] The observations can be explained by five different models, four that are associated with very small particles having sizes less than 10 μm (droxtal-4 μm, droxtal-6 μm, columns-b, compacts-c), and one (MODIS-rough) that corresponds to larger mean size (30 μm) containing a mixture of different shapes (bullet rosettes, plates and hollow columns) having rough surfaces. The spherical models, even if associated with small sizes cannot explain the measurements. For 3 of the 5 days under study (23, 26,

and 29 July) the small simple hexagonal columns model is the best candidate for explaining the observations as R_{CAS} ranges from 115 to 123. For 11 July the measured R_{CAS} values are highly variable. However, for the measurements that are collocated with satellite observations, $R_{CAS} = 111$ which is close to the MODIS-rough model value.

5. Comparisons Between Remote Sensing and in Situ Results

5.1. Comparison Between Dual Satellites and CAS Results

[26] The 11 July satellite and in situ observations are well correlated in space and time. Of course, the WB57F flies within the cloud at a constant altitude, whereas satellite observations are sensitive to a vertically integrated thickness of cloud. The in situ and satellite analyses use different viewing directions but they are based on the same scattering phase function. Under the assumption that the altitude level flown by the aircraft is representative of the vertical depth sounded by the satellite, the results can be compared.

[27] The satellite and in situ retrievals give consistent results for two of the four areas (Z1 and Z2), where the column model is judged most appropriate. The inconsistency between satellite and in situ retrievals for the first area (Z0) can be explained by the fact that the shape retrieved from the in situ data (Figure 6) is strongly variable in time for that day at Z0 time. The satellite retrieval was averaged over 36×36 km^2 around the WB57F flight track and cannot capture the smaller-scale variability seen in Figure 6 that is associated with a short descent of 1 km within the cloud. For area Z3, the inconsistency might be explained by the time difference between the satellite and in situ retrievals, which reaches a maximum of 20 min.

5.2. Comparison Between Lidar and CAS Results

[28] Following the lidar, five segments among thirteen are dominated by shape ratios larger than unity (segments 4, 5, 6, 7 of 23 July, and segment 4 of 26 July) that are associated with hexagonal columns. For those segments, the results are consistent with the R_{CAS} observations that also indicate small hexagonal columns.

[29] For segment 3 of 23 July, the lidar retrieval produces results suggesting the presence of many different particle shapes without clear dominance of any one particle type whereas the CAS gives results ranging between columns and droxtals.

[30] For segments 1 and 2 of 26 July and segment 1 of 29 July, the lidar retrieval indicates hexagonal plates (shape ratio lower than 1) or spherical particles, whereas the in situ data correspond to small columns. This discrepancy could be due to the cloud spatial heterogeneities that appear in Figures 2b and 2c. In those areas, the in situ sensor has difficulty retrieving the particle shape because the sensor does not encounter a sufficient quantity of particles. For example, Figure 6 shows that the values of the in situ ratio for those three segments are interpolated (in line) and not retrieved (in dot).

[31] For segment 3 of 26 July, the lidar data show a dominance of hexagonal compact (unity shape ratio) whereas the in situ obtains small hexagonal columns. This segment

Table 3a. Summary of Results Derived From Satellite and In Situ Data

Date	Satellites		In Situ	
Date	Area	???????	Ratio	Shape
11 July	Z0	columns	111	MODIS_rough
11 July	Z1	columns	116	columns-b
11 July	Z2	columns	119	columns-b
11 July	Z3	spheres	119	columns-b

Table 3c. Summary of Results Derived From Lidar and Satellite Data[a]

Date	Lidar				Satellites
Date	Area	???	???	???	???	Satellites
23 July	Z1	22	**59**	11	8	columns
23 July	Z2	**45**	44	4	6	spheres
29 July	Z1	36	**47**	13	4	plates/BR/MODIS-1/MODIS-2

[a]Boldface indicates more probable particle type.

corresponds to a 2-km descent of the WB57 within a thick cloud. As shown in Figure 2b, the lidar depolarization value changes within the cloud along the WB57 trajectory, leading to various particle shapes, producing, in the mean, a dominance of hexagonal compacts. On the contrary, the in situ retrieval is quite constant along this trajectory (Figure 6), explained by the capability of the CAS to observe only particles smaller than 45 μm whereas the lidar retrieval is influenced by larger particles having different shape ratios.

[32] For the last two segments (1 and 2 of 23 July), the lidar results give hexagonal plates and spheres whereas the CAS indicates small hexagonal columns. This discrepancy may be due to both the small time period considered (2 and 4 min, respectively, see Table 3) and the cloud spatial heterogeneities in this area (Figure 2a).

5.3. Comparisons Between Dual-Satellite and Lidar Results

[33] Among the three cloud areas used to compare lidar and satellite results, two give consistent results and one does not. For the 23 July area Z2, the lidar retrieval is dominated by spheres or plate-like particles and the satellite retrieval is close to spheres. For 29 July, the lidar retrieval indicates mostly plates (shape ratio lower than 1), whereas the satellite retrieval is ambiguous with four possible solutions: plates, bullet rosettes and MODIS-1 and MODIS-2 models that consist of a mixture of plates, bullet rosettes and hollow columns. The inconsistency obtained for area Z1 of 23 July (lidar gives plates whereas satellite gives columns) may be due the 15-min difference between the two satellite observations that necessitated averaging the data over 36 ×

36 km (Figure 4b) and to the 12 min time difference between the satellite and lidar observations.

6. Discussion and Conclusion

[34] In total, 40 ice crystal shape retrievals have been processed using three different methods, and compared two by two leading to 20 intercomparisons: four satellite with in situ, 13 lidar with in situ, and three satellite with lidar. Nine of the comparisons give consistent results, two have mixed lidar retrievals that cannot be interpreted for the comparisons, and nine cases give inconsistent results. Those inconsistencies can be partially explained as follows.

[35] In two cases, the spatial-temporal matching of the data appears to be insufficient: the time difference between the two satellites is large (15 min) and the comparative measurements (one lidar, one in situ), are taken 15 min before or after the two satellite images. The development and dissipation of anvils during CF were generally quite rapid and the clouds typically advected westward. Thus the sampled fields can be quite different when the measurements are taken 15-min apart.

[36] In two cases, the lidar retrievals are applied to a data set that is too short to be representative in a spatially heterogeneous cloud.

[37] In one case, the in situ retrieval is performed using data along a descent of the WB57F within the cloud leading to a large variation in shapes that is smoothed out by the large averaging area of the satellite measurements.

[38] In one case, the in situ retrieval is along an ascent of the WB57F within the cloud showing variability with altitude in the lidar retrieval but not in the in situ data. That

Table 3b. Summary of Results Derived From Lidar and In Situ Data[a]

Date	UT	Lidar				In Situ	
Date	UT	$Q < 0.05$ Spheres,[b] %	$0.05 < Q < 0.7$,[b] %	$0.7 < Q < 1.05$,[b] %	$Q > 1.05$,[b] %	Ratio	Shape
23 July	1972–1974	16	**75**	7	2	117	columns-B
	1978–1982	**40**	32	8	20	117	columns-B
	2023–2032	14	25	**32**	29	117	columns-B
	2116–2122	15	20	28	**37**	117	columns-B
	2167–2175	20	25	25	**30**	119	columns-B
	2216–2217	12	13	0	**75**	119	columns-B
	2257–2262	27	25	16	**32**	119	columns-B
	2305–2320	22	**32**	25	21	121	columns-B
26 July	1740–1743	**90**	10	0	0	121	columns-B
	1828–1851	6	7	**68**	19	121	columns-B
	1901–1914	2	20	**61**	17	121	columns-B
	1916–1921	1	7	**49**	43	121	columns-B
29 July	1988–1993	23	**43**	20	14	121	columns-B

[a]Boldface indicates more probable particle type.
[b]Here $1 \geq Q \geq 0.7$ corresponds to plate-c and compact-b. $Q = 0.05$ corresponds to plate-b. $Q \geq 1$ corresponds to columns, compacts, CERES-Big, and CERES-Nov1.

may be a result of the limited size range of the CAS whereas the lidar retrieval is influenced by all the particles sizes.

[39] Hence, among the nine cases showing disagreement, seven are likely due to poor spatial-temporal matching and two are a result of the physical limitations of the retrieval method. Moreover, the CAS retrieval gives information on the particle shape for particles smaller than 45 μm only. This is not necessarily a limitation as there are very few in situ methods that provide shape information for these very small particles; however, when large particles are present, the CAS might not provide a representative assessment of the particle shapes for the entire sampling space.

[40] Finally, the results obtained in this study are encouraging as the method of using two remote sensors contains valuable information on the particle shape for ice crystals having sizes smaller than 45 μm. Nevertheless, the use of these methods requires some precautions. The dual satellite method has to be applied only when the satellite time difference is small enough (typically less than 15 min) and averages over several pixels (at least 20 km super pixels) can be computed (i.e., the cloud must be large enough). The lidar retrieval seems to be robust only if applied to data averaged over several minutes within well-formed clouds without strong spatial inhomogeneities.

[41] The remote sensing and in situ techniques all agree in the rejection of a large fraction of the 20 optical property models considered at the beginning of the study (Table 2) and conclude that for the different cloud cases examined here the columns, bullet rosettes, spheres, plates, droxtal and mixtures of those (MODIS-rough models) are the best candidates. In this sense the three methods are quite consistent but it does not mean that these shapes are necessarily the dominant ones during CF. Other studies, each using only one of the current methods on the complete CF data set [*Baumgardner et al.*, 2005; *Noel et al.*, 2004], indicate that the shape variability is considerably larger than that found here. Vertically, the cloud particle sizes and shapes within a cirrus or anvil cloud can be highly variable [e.g., *Garrett et al.*, 2005] and were not often sampled by the WB57F because most of its flight legs were level at very high altitudes and primarily sampled either the tops of the anvils or the very thin cirrus clouds that often formed above the anvil. In those areas, especially in the thin cirrus, small particles dominate the spectrum and may not necessarily represent the vertically integrated microphysical structure of the clouds. Thus it is surprising that the satellite and in situ data agree as well as they do.

[42] Nevertheless, these results show that the lidar has the potential to give quantitative results about the particle shape (or asymmetry factor) on a systematic basis, thus providing information on the vertical variability of the ice crystal shape within the cloud itself. Progress can be made by including more optical models associated with different shapes and sizes in order to approach more realistic crystal habits (or asymmetry factors) rather than four different large classes. As shown in Table 2, however, the main limitation in this approach comes from the lack of ice crystal models with the complete scattering matrix in the backscattering direction. Even without additional models, the application of the lidar method to the future Cloud-Aerosol Lidar and Infrared Pathfinder (CALIPSO) [see *Winker et al.*, 2003] mission global lidar data set could provide a rough estimate of the variability of ice crystal shape within the cloud at the different latitudes along the satellite track. Such information would represent a large step beyond our current understanding of crystal habits, even if the data do not correspond to the "real" shape as given by in situ observations.

[43] The dual satellite method contains potentially valuable information to discriminate the scattering phase function in the visible domain that is mainly a signature of the particle shape because of the angles considered. This method has an advantage in that it can be used to test all the optical properties available in the literature since it only requires the scattering phase function. Hence all 20 models presented in Table 2 were tested and new ones can be included with no limitations as they become available. This method requires good collocation in space and time between the two satellites and a robust treatment of their visible-channel calibrations. On one hand, these two constraints require heavy pretreatment of the satellite data for extensive applications, but on the other hand this method could be applied to the large existing data set and comprises the visible-channel data from most operational and research satellite imagers. Analysis of those data would yield valuable new information on the spatial and temporal variability of the particle asymmetry factor. This technique is also ideal for application to data from satellite-borne multiangle view scanners, like the Multiangle Imaging Spectroradiometer (MISR) [see *Diner et al.* [2000] that view a given scene from more than one angle during a given overpass.

[44] In addition to logistical, matching, and calibration concerns, a variety of studies should be performed to better understand the retrievals. The sensitivity of the dual satellite method to vertical variations in ice crystal shape and size should be explored to determine what portion of the cloud is represented by the retrieval. Additional in situ data should be taken using vertical profiles that are coincident with the dual-satellite or MISR overpasses using sensors that cover a wide range of particle sizes. Expert mission planning is essential for achieving that goal. The additional data would also help unravel the results of the lidar retrieval in order to better define shapes from the depolarization ratios. Coincident data sets from future field missions similar to CF and from Aqua and CALIPSO will be essential for enhancing the value of the remote sensing methods examined here.

References

Auer, A. H., Jr., and D. L. Veal (1970), The dimension of ice crystals in natural clouds, *J. Atmos. Sci.*, *27*, 919–926.

Baran, A. J., S. J. Brown, J. S. Foot, and D. L. Mitchell (1999), Retrieval of tropical cirrus thermal optical depth, crystal size and shape using a dual view instrument at 3.7 μm and 10.8 μm, *J. Atmos. Sci.*, *52*, 4246–4263.

Baum, B. A., D. P. Kratz, P. Yang, S. C. Ou, Y. Hu, P. Soulen, and S.-C. Tsay (2000), Remote sensing of cloud properties using MODIS airborne simulator imagery during SUCCESS: 1. Data and models, *J. Geophys. Res.*, *105*, 11,767–11,780.

Baumgardner, D., H. Jonsson, W. Dawson, D. O'Connor, and R. Newton (2001), The cloud, aerosol and precipitation spectrometer: A new instrument for cloud investigations, *Atmos. Res.*, *59–60*, 251–264.

Baumgardner, D., H. Chepfer, G. B. Raga, and G. L. Kok (2005), The shapes of very small cirrus particles derived from in situ measurements, *Geophys. Res. Lett.*, *32*, L01806, doi:10.1029/2004GL021300.

Chepfer, H., G. Brogniez, and Y. Fouquart (1998), Cirrus clouds microphysical properties deduced from POLDER observations, *J. Quant. Spectrosc. Radiat. Transfer*, *60*, 375–390.

Chepfer, H., P. Goloub, J. Riedi, J. De Haan, J. W. Hovenier, and P. H. Flamant (2001), Ice crystal shapes in cirrus clouds derived from POLDER/ADEOS-1, *J. Geophys. Res.*, *106*, 7955–7966.

Chepfer, H., P. Minnis, D. Young, L. Nguyen, and R. F. Arduini (2002), Estimation of cirrus cloud effective ice crystal shapes using visible reflectances from dual-satellite measurements, *J. Geophys. Res.*, *107*(D23), 4730, doi:10.1029/2000JD000240.

De Haan, J., P. B. Bosma, and J. W. Hovenier (1986), The adding method for multiple scattering of polarized light, *Astron. Astrophys.*, *183*, 371–391.

Diner, D. J., J. C. Beckert, G. W. Bothwell, and J. I. Rodriguez (2000), Performance of the MISR instrument during its first 20 months in Earth orbit, *IEEE Trans. Geosci. Remote Sens.*, *40*, 1449–1466.

Eberhard, W. L. (1992), Ice-cloud depolarization of backscatter CO_2 and other infrared lidars, *Appl. Opt.*, *31*, 6485–6490.

Eloranta, E. W. (1998), A practical model for the calculation of multiply scattered lidar returns, *Appl. Opt.*, *37*, 2464–2472.

Francis, P. N., A. Jones, R. W. Saunders, K. P. Shine, A. Slingo, and Z. Sun (1994), An observational and theoretical study of the radiative properties of cirrus: Some results from ICE'89, *Q. J. R. Meteorol. Soc.*, *120*, 809–848.

Garrett, T. J., H. Gerber, D. G. Baumgardner, C. H. Twohy, and E. M. Weinstock (2003), Small, highly reflective ice crystals in low-latitude cirrus, *Geophys. Res. Lett.*, *30*(21), 2132, doi:10.1029/2003GL018153.

Garrett, T. J., et al. (2005), In situ measurements of the microphysical and radiative evolution of a Florida cirrus anvil, *J. Atmos. Sci.*, in press.

Haeffelin, M., et al. (2005), SIRTA, a French atmospheric observatory for clouds, aerosols and water vapor, *Ann. Geophys.*, *23*, 253–275.

Heymsfield, A. J. (1975), Cirrus uncinus generating cells and the evolution of cirriform clouds. part I: Aircraft observations of the growth of the ice phase, *J. Atmos. Sci.*, *32*, 799–807.

Heymsfield, A. J. (1993), Microphysical structure of stratiform and cirrus clouds, in *Aerosol–Cloud–Climate Interactions*, *Int. Geophys. Ser.*, vol. 54, edited by P. V. Hobbs, pp. 97–119, Elsevier, New York.

Heymsfield, A. J., and C. M. R. Platt (1984), A parameterization of the particle size spectrum of ice clouds in terms of the ambient temperature and the ice water content, *J. Atmos. Sci.*, *41*, 846–855.

Hu, Y., D. Winker, P. Yang, B. Baum, L. Poole, and L. Vann (2001), Identification of cloud phase from PICASSO-CENA lidar depolarization: A multiple scattering sensitivity study, *J. Quant. Spectrosc. Radiat. Transfer*, *70*, 569–579.

Inoue, T. (1985), On the temperature and the effective emissivity determination of semi-transparent clouds by bi-spectral measurements in the 10 μm window region, *J. Meteorol. Soc. Jpn.*, *63*, 88–98.

Intrieri, J. M., G. L. Stephens, W. L. Eberhard, and T. Uttal (1993), A method for determining cirrus cloud particle sizes using lidar and radar backscatter technique, *J. Appl. Meteorol.*, *32*, 1074–1082.

Jensen, E., D. Starr, and O. Toon (2004), Mission investigates tropical cirrus clouds, *Eos Trans. AGU*, *85*(5), 45, 50.

King, M. D., W. P. Menzel, Y. J. Kaufman, D. Tanre, B. C. Gao, S. Platnick, S. A. Ackerman, L. A. Remer, R. Pincus, and P. A. Hubanks (2003), Cloud and aerosol properties, precipitable water, and profiles of temperature and humidity from MODIS, *IEEE Trans. Geosci. Remote Sens.*, *41*, 442–458.

King, M. D., S. Platnick, P. Yang, G. T. Arnold, M. A. Gray, J. C. Riédi, S. A. Ackerman, and K. N. Liou (2004), Remote sensing of liquid water and ice cloud optical thickness, and effective radius in the Arctic: Application of airborne multispectral MAS data, *J. Atmos. Oceanic Technol.*, *21*, 857–875.

Korolev, G. A., and I. J. Hallett (2000), Ice particle habits in stratiform clouds, *Q. J. R. Meteorol. Soc.*, *126*, 2873–2902.

Liou, K. N. (1986), Influence of cirrus clouds on weather and climate processes: A global perspective, *Mon. Weather Rev.*, *114*, 1167–1199.

Mace, G. G., A. J. Heymsfield, and M. R. Poellot (2002), On retrieving the microphysical properties of cirrus clouds using the moments of the millimeter-wavelength Doppler spectrum, *J. Geophys. Res.*, *107*(D24), 4815, doi:10.1029/2001JD001308.

Macke, A. (1993), Scattering of light by polyhedral ice crystals, *Appl. Opt.*, *32*, 2780–2788.

Macke, A., J. Mueller, and E. Raschke (1996), Single scattering properties of atmospheric ice crystals, *J. Atmos. Sci.*, *53*, 2813–2825.

Masuda, K., H. Ishimoto, and T. Takashima (2002), Retrieval of cirrus optical thickness and ice-shape information using total and polarized

reflectance from satellite measurements, *J. Quant. Spectrosc. Radiat. Transfer*, *75*, 39–51.

McFarquhar, G. M., and A. J. Heymsfield (1996), Microphysical characteristics of three cirrus anvils sampled during the Central Equatorial Pacific Experiment (CEPEX), *J. Atmos. Sci.*, *52*, 2401–2423.

McGill, M. J., L. Li, W. D. Hart, G. M. Heymsfield, D. L. Hlavka, P. E. Racette, L. Tian, M. A. Vaughan, and D. M. Winker (2004), Combined lidar-radar remote sensing: Initial results from CRYSTAL-FACE, *J. Geophys. Res.*, *109*, D07203, doi:10.1029/2003JD004030.

Minnis, P., P. W. Heck, and D. F. Young (1993), Inference of cirrus cloud properties using satellite-observed visible and infrared radiances. part II: Verification of theoretical cirrus radiative properties, *J. Atmos. Sci.*, *50*, 1305–1322.

Minnis, P., D. P. Garber, D. F. Young, R. F. Arduini, and Y. Takano (1998), Parameterizations of reflectance and effective emittance for satellite remote sensing of cloud properties, *J. Atmos. Sci.*, *55*, 3313–3339.

Minnis, P., L. Nguyen, D. R. Doelling, D. F. Young, W. F. Miller, and D. P. Kratz (2002), Rapid calibration of operational and research meteorological satellite imagers, part I: Evaluation of research satellite visible channels as references, *J. Atmos. Oceanic Technol.*, *19*, 1233–1249.

Mishchenko, M. I., and K. Sassen (1998), Depolarization of lidar returns by small ice crystals: An application to contrails, *Geophys. Res. Lett.*, *25*, 309–312.

Noel, V., G. Ledanois, H. Chepfer, and P. H. Flamant (2001), Computation of single-scattering matrix for nonspherical particles randomly or horizontally oriented in space, *Appl. Opt.*, *40*, 4365–4375.

Noel, V., H. Chepfer, G. Ledanois, A. Delaval, and P. H. Flamant (2002), Classification of effective shape ratios in cirrus clouds based on lidar depolarization ratio, *Appl. Opt.*, *41*, 4245–4257.

Noel, V., D. M. Winker, M. McGill, and P. Lawson (2004), Classification of particle shapes from lidar depolarization ratio in convective ice clouds compared to in situ observations during CRYSTAL-FACE, *J. Geophys. Res.*, *109*, D24213, doi:10.1029/2004JD004883.

Pal, S. R., and A. I. Carswell (1976), The polarization characteristics of lidar scattering from snow and ice crystals in the atmosphere, *J. Appl. Meteorol.*, *16*, 70–80.

Platnick, S., M. D. King, S. A. Ackerman, W. P. Menzel, B. A. Baum, J. C. Riédi, and R. A. Frey (2003), The MODIS cloud products: Algorithms and examples from Terra, *IEEE Trans. Geosci. Remote Sens.*, *41*, 459–473.

Platt, C. M. R. (1977), Lidar observations of a mixed-phase altostratus cloud, *J. Appl. Meteorol.*, *16*, 339–345.

Platt, C. M. R., N. L. Abshire, and G. T. McNice (1978), Some microphysical properties of an ice cloud from lidar observations of horizontally oriented crystals, *J. Appl. Meteorol.*, *17*, 1220–1224.

Randall, D., B. Albrecht, S. Cox, D. Johnson, P. Minnis, W. Rossow, and D. Starr (1996), On FIRE at ten, *Adv. Geophys.*, *38*, 37–177.

Raschke, E., P. Flamant, Y. Fouquart, P. Hignett, H. Isaka, P. R. Jonas, H. Sundquist, and P. Wendling (1998), Cloud radiation studies during the European Cloud Radiation Experiment (EUCREX), *Surv. Geophys.*, *19*, 89–138.

Sassen, K. (1991), The polarization lidar technique for cloud research: A review and current assessment, *Bull. Am. Meteorol. Soc.*, *72*, 1848–1866.

Stefanutti, L., M. Morandini, M. Del Guasta, S. Godin, and C. David (1995), Unusual PCSs observed by lidar in Antarctica, *Geophys. Res. Lett.*, *22*, 2377–2380.

Stephens, G. L., S. C. Tsay, P. W. Stackhouse Jr., and P. J. Flateau (1990), The relevance of the microphysical and radiative properties of cirrus clouds to the climate and climatic feedback, *J. Atmos. Sci.*, *47*, 1742–1753.

Takano, Y., and K. N. Liou (1989), Solar radiative transfer in cirrus clouds. part I: Single-scattering and optical properties of hexagonal ice crystals, *J. Atmos. Sci.*, *46*, 3–19.

Thuman, W. C., and E. Robinson (1954), Studies of Alaskan ice-fog particles, *J. Meteorol.*, *11*, 151–156.

Toon, O. B., and R. C. Miake-Lye (1998), Subsonic Aircraft: Contrail and Cloud Effects Special Study (SUCCESS), *Geophys. Res. Lett.*, *25*, 1109–1112.

Wendling, P., R. Wendling, and H. K. Weickmann (1979), Scattering of solar radiation by hexagonal ice crystals, *Appl. Opt.*, *18*, 2663–2671.

Winker, D. M., J. Pelon, and M. P. McCormick (2003), The CALIPSO mission: Spaceborne lidar for observation of aerosols and clouds, *Proc. SPIE Int. Soc. Opt. Eng.*, *4893*, 1–11.

Yang, P., and K. N. Liou (1996), Geometric-optics-integral-equation method for light scattering by nonspherical ice crystals, *Appl. Opt.*, *35*, 6568–6584.

Yang, P., and K. N. Liou (1998), Single scattering properties of complex ice crystals in terrestrial atmosphere, *Contrib. Atmos. Phys.*, *71*, 223–248.

Yang, P., B. A. Baum, A. J. Heymsfield, Y. X. Hu, H.-L. Huang, S.-C. Tsay, and S. Ackerman (2003), Single-scattering properties of droxtals, *J. Quant. Spectrosc. Radiat. Transfer*, *79–80*, 1159–1180.

Zhang, Z., P. Yang, G. W. Kattawar, S.-C. Tsay, B. A. Baum, H.-L. Huang, Y. X. Hu, A. J. Heymsfield, and J. Reichardt (2004), Geometric optics solution to light scattering by droxtal ice crystals, *Appl. Opt.*, *43*, 2490–2499.

————————————————

D. Baumgardner and G. Raga, Universidad Nacional Autónoma de México, Mexico City 04510, Mexico.

H. Chepfer, Laboratoire de Météorologie Dynamique, Institut Pierre-Simon Laplace, Ecole Polytechnique, Palaiseau F-91128, France. (chepfer@lmd.polytechnique.fr)

M. J. McGill, NASA Goddard Space Flight Center, Code 613.1 Building 33, Greenbelt, MD 20771, USA.

P. Minnis and L. Nguyen, NASA Langley Research Center, MS 420, Hampton, VA 23681, USA.

V. Noel, Analytical Services and Materials, Inc., 107 Research Drive, Hampton, VA 23666, USA.

P. Yang, Department of Atmospheric Sciences, Texas A&M University, College Station, TX 77843, USA.